

Northumbria Research Link

Citation: Tiwari, Ajay, Morton, Richard and McLaughlin, James (2021) A Statistical Study of Propagating MHD Kink Waves in the Quiescent Corona. The Astrophysical Journal, 919 (2). p. 74. ISSN 0004-637X

Published by: IOP Publishing

URL: <https://doi.org/10.3847/1538-4357/ac10c4> <<https://doi.org/10.3847/1538-4357/ac10c4>>

This version was downloaded from Northumbria Research Link:
<https://nrl.northumbria.ac.uk/id/eprint/47402/>

Northumbria University has developed Northumbria Research Link (NRL) to enable users to access the University's research output. Copyright © and moral rights for items on NRL are retained by the individual author(s) and/or other copyright owners. Single copies of full items can be reproduced, displayed or performed, and given to third parties in any format or medium for personal research or study, educational, or not-for-profit purposes without prior permission or charge, provided the authors, title and full bibliographic details are given, as well as a hyperlink and/or URL to the original metadata page. The content must not be changed in any way. Full items must not be sold commercially in any format or medium without formal permission of the copyright holder. The full policy is available online: <http://nrl.northumbria.ac.uk/policies.html>

This document may differ from the final, published version of the research and has been made available online in accordance with publisher policies. To read and/or cite from the published version of the research, please visit the publisher's website (a subscription may be required.)



**Northumbria
University**
NEWCASTLE



UniversityLibrary



A Statistical Study of Propagating MHD Kink Waves in the Quiescent Corona

Ajay K. Tiwari^{1,2} , Richard J. Morton¹ , and James A. McLaughlin¹ ¹Northumbria University Newcastle upon Tyne, NE1 8ST, UK; ajaynld13@gmail.com²Centrum Wiskunde & Informatica, Amsterdam, 1098 XG Amsterdam, The Netherlands

Received 2021 May 26; revised 2021 June 30; accepted 2021 June 30; published 2021 September 28

Abstract

The Coronal Multi-channel Polarimeter (CoMP) has opened up exciting opportunities to probe transverse MHD waves in the Sun's corona. The archive of CoMP data is utilized to generate a catalog of quiescent coronal loops that can be used for studying propagating kink waves. The catalog contains 120 loops observed between 2012 and 2014. This catalog is further used to undertake a statistical study of propagating kink waves in the quiet regions of the solar corona, investigating phase speeds, loop lengths, footpoint power ratio (a measure of wave power entering the corona through each footpoint of a loop) and equilibrium parameter (which provides a measure of the change in wave amplitude) values. The statistical study enables us to establish the presence of a relationship between the rate of damping and the length of the coronal loop, with longer coronal loops displaying weaker wave damping. We suggest the reason for this behavior is related to a decreasing average density contrast between the loop and ambient plasma as loop length increases. The catalog presented here will provide the community with the foundation for the further study of propagating kink waves in the quiet solar corona.

Unified Astronomy Thesaurus concepts: [Magnetohydrodynamics \(1964\)](#); [Quiet solar corona \(1992\)](#); [Solar coronal loops \(1485\)](#); [Solar coronal heating \(1989\)](#); [Quiet sun \(1322\)](#); [Solar activity \(1475\)](#)

Supporting material: machine-readable table

1. Introduction

The presence of MHD waves in the solar atmosphere is now well established (e.g., Ofman et al. 1997; DeForest & Gurman 1998; Erdélyi et al. 1998; Aschwanden et al. 1999; Nakariakov et al. 1999; Schrijver et al. 1999; De Moortel et al. 2000; Williams et al. 2001, 2002; Goossens et al. 2002; Marsh et al. 2002; Ofman & Aschwanden 2002; Katsiyannis et al. 2003; Wang et al. 2003; Verwichte et al. 2005; Tomczyk et al. 2007; Tomczyk & McIntosh 2009; Morton et al. 2012, 2016, 2019). Of all the MHD wave modes observed in the solar atmosphere, some of the most interesting are the transverse waves. They are thought to be critical in transferring energy from the turbulent convection in the photosphere to the solar corona.

The most common transverse wave in the corona appears to be the kink mode (the presence of torsional modes are more difficult to determine; however, there is some evidence for such motions, e.g., Kohutova et al. (2020)). The kink mode has, to date, been observed in the corona in three variants: (*decaying*) *standing* kink waves, *decay-less* standing kink waves, and *propagating* kink waves. The standing kink waves were the first transverse wave modes to be observed in active region coronal loops (Aschwanden et al. 1999; Nakariakov et al. 1999), found with the Transition Region and Coronal Explorer (Handy et al. 1999). These observations, and the launch of the Solar Dynamics Observatory (SDO; Pesnell et al. 2012), heralded a new era in the exploration and understanding of the physical properties of the solar corona through standing kink modes (Nakariakov & Kolotkov 2020). The standing kink modes are typically observed in active region coronal loops

following an eruptive process (Stepanov et al. 2012; Zimovets & Nakariakov 2015; Goddard et al. 2016). The excitation mechanism of these standing kink waves is believed to be nearby eruptions or plasma ejections (rather than a blast shock wave ignited by a flare, as previously thought, e.g., Zimovets & Nakariakov 2015), which leads to a displacement of the coronal loops from their equilibrium position. These waves are found to be rapidly damped, with the damping being attributed to the phenomenon of resonant absorption or mode coupling (e.g., Ionson 1978; Hollweg 1984; Goossens et al. 2002; Ruderman & Roberts 2002; Aschwanden et al. 2003). More recently, Goddard et al. (2016) produced a catalog of standing kink modes observed with the SDO Atmospheric Imaging Assembly (AIA; Lemen et al. 2012), which was later extended by Nechaeva et al. (2019). A study of the relationship between damping time and amplitude indicated that a nonlinear damping mechanism might also contribute to the observed damping. Van Doorsselaere et al. (2021) suggested that the observed relationship could be explained by uni-turbulence, a form of generalized phase mixing (Magyar et al. 2019; Van Doorsselaere et al. 2020).

Second, there has been the discovery of decay-less standing kink wave modes (Tian et al. 2012; Wang et al. 2012; Anfinogentov et al. 2013, 2015; Nisticò et al. 2013) in active region loops. These low-amplitude (<1 Mm) oscillations do not appear to damp in time and are seen for several cycles. In some cases, the wave amplitudes are shown to gradually grow (e.g., Wang et al. 2012).

Finally, it has been demonstrated that there are persistent and ubiquitous fluctuations in the Doppler velocities of coronal emission lines, which propagate at Alfvénic speeds and follow magnetic field lines (Tomczyk et al. 2007; Morton et al. 2019; Yang et al. 2020a, 2020b). These motions have been interpreted as propagating kink waves and have also been observed with SDO/AIA (e.g., McIntosh et al. 2011; Thurgood et al. 2014; Weber et al. 2018, 2020). There have been several



Original content from this work may be used under the terms of the [Creative Commons Attribution 4.0 licence](#). Any further distribution of this work must maintain attribution to the author(s) and the title of the work, journal citation and DOI.

studies to reveal the properties of the propagating kink waves, finding that the power spectra of the velocity fluctuations can be described with a power law, and also show an enhancement of power at 4 mHz (e.g., Tomczyk & McIntosh 2009; Morton et al. 2015, 2016, 2019). The excitation mechanism for the propagating waves is believed to be the random shuffling of magnetic elements in the photosphere due to convection, although this mechanism appears only to be able to explain the high-frequency part of the observed power spectrum (Cranmer & Van Ballegoijen 2005). Observational and theoretical studies provide evidence that indicates that mode conversion of p -modes may play a role in exciting some fraction of the observed waves (Cally 2017; Morton et al. 2019). Moreover, the origin of the low-frequency velocity fluctuations is still unclear, although Cranmer (2018) suggests that reconnection resulting from the evolution of the magnetic carpet may be the source.

The damping and dissipation of the propagating kink waves have not yet received as much attention as the standing modes. In the case of the propagating kink waves, to date there has only been a single observational case study analyzed in the literature. Verth et al. (2010) were the first to highlight the wave damping of the waves along the coronal loop presented in Tomczyk & McIntosh (2009), suggesting resonant absorption could provide a reasonable description of the observed behavior. A number of other studies have also used the same event for similar investigations into wave damping (e.g., Verwichte et al. 2013b; Pascoe et al. 2015; Tiwari et al. 2019; Montes-Solis & Arregui 2020).

The focus of many previous studies has been on the (decaying and decay-less) standing kink waves observed in active regions, with many statistical studies revealing the typical properties of these modes (e.g., Anfinogentov et al. 2015; Nechaeva et al. 2019). Given that the quiescent corona occupies a larger volume of the Sun's atmosphere than active regions and is omnipresent over the solar cycle, it is vital to understand the nature of the propagating kink waves that exist there and the waves' role in heating the quiescent coronal plasma. However, to date, there has been little focus on the propagating kink waves observed in quiescent corona. This paper attempts to fill some of that gap in our knowledge and provides a catalog of suitable quiescent coronal loops that can be used for studying the propagating kink waves. In generating this catalog, an overview of some of the typical propagating kink wave properties in the quiescent Sun is also provided. This paper also serves as a natural extension to the study by Tiwari et al. (2019).

The paper is structured as follows: In Section 2 the details of data and the analysis methods used are provided. Section 3 presents the main results and discusses the findings. The paper is concluded in Section 4.

2. Data and Analysis

2.1. Observations

The data are obtained from the Coronal Multi-channel Polarimeter (CoMP; Tomczyk et al. 2008), a coronagraph that observes the off-limb corona between 1.05 and $1.35 R_{\odot}$. CoMP is an imaging spectro-polarimeter, and provides images of the corona taken at three different wavelength positions centered on the 10747 \AA Fe XIII coronal emission line (referred to as three-point measurements). The data were selected from CoMP

observations taken between 2012 and 2016. The data sets consisting of more than 135 (near)-contiguous data frames are identified by a manual inspection of the CoMP online data archive.³ The specific dates are given in Table 2. The data sets from each selected date have a temporal cadence of 30 s (some with a small number of missing frames, <5%) and spatial sampling of $\sim 4.5''$. The Doppler velocity data products derived from fitting a Gaussian model to the line profile from the three-point measurements are the focus of this study. Details of the procedure used to estimate the Doppler velocities are given in Tian et al. (2013), and an assessment of their uncertainties is performed in Morton et al. (2016). A time series of Doppler velocity images of the corona is used for this study. In cases where frames are missing, linear interpolation is performed to fill the gaps. Further registration of the Doppler images within each time sequence is undertaken via cross correlation, with further details given in Morton et al. (2016).

The analysis of the propagating kink waves requires the measurement of the wave propagation direction. Hence, a data product called a *wave angle map* is also derived, which gives the relative direction of propagation for the velocity signal within each pixel. The basis of the wave angle calculation requires a coherence-based approach for the analysis of the velocity signals. General details of the method are discussed in McIntosh et al. (2008) and particular applications to CoMP data are discussed in Tomczyk & McIntosh (2009), Morton et al. (2015), and Tiwari et al. (2019). The strategy is to use the coherence between the Doppler velocity time series of each pixel and its neighboring pixels to obtain islands of coherence above a threshold value. The direction of wave propagation is calculated by a straight line fit through the islands, which minimizes the sum of perpendicular distances from the points to the line. Performing this operation for each pixel of the Doppler velocity images gives the wave angle map. A sample wave angle map is shown in the center panel of Figure 1.

2.2. Selection of Loops for Study

The selection of the loops from the CoMP data is a critical step in the analysis of the waves. For each of the data sets, suitable systems of coronal loops are identified. A lower limit of 50 Mm is placed on the lengths of the loop systems selected, whereby length refers to their visible length in the CoMP field of view (FOV).⁴ This limit is required to preserve a high signal-to-noise level in the Doppler velocity time series. Smaller loops are closer to the occulting disk, where the signal suffers from a high scattering of photons that leads to poor estimates for the Doppler velocity and hence increased noise in time series. The imposition of a minimum loop length also ensures an appropriate sampling in the k direction in Fourier space, which is required for further analysis. A few such selected loops are shown in the right panel of Figure 1. The loops are chosen by manually identifying closed-loop structures first in the Doppler and intensity image sequences and later also in the wave angle map. The closed-loop structures as arcades of loops that appear semicircular are identified, with each leg starting near the occulting disk.

³ https://mlso.hao.ucar.edu/mlso_data_calendar.php?calinst=comp

⁴ An issue with measurements of the absolute length of loops is that the occulter on CoMP covers the solar disk out to $\sim 1.05 R_{\odot}$, meaning that it is not possible to trace the coronal loops back to their footpoints. Hence, only the length of the loop in the CoMP FOV is reported.

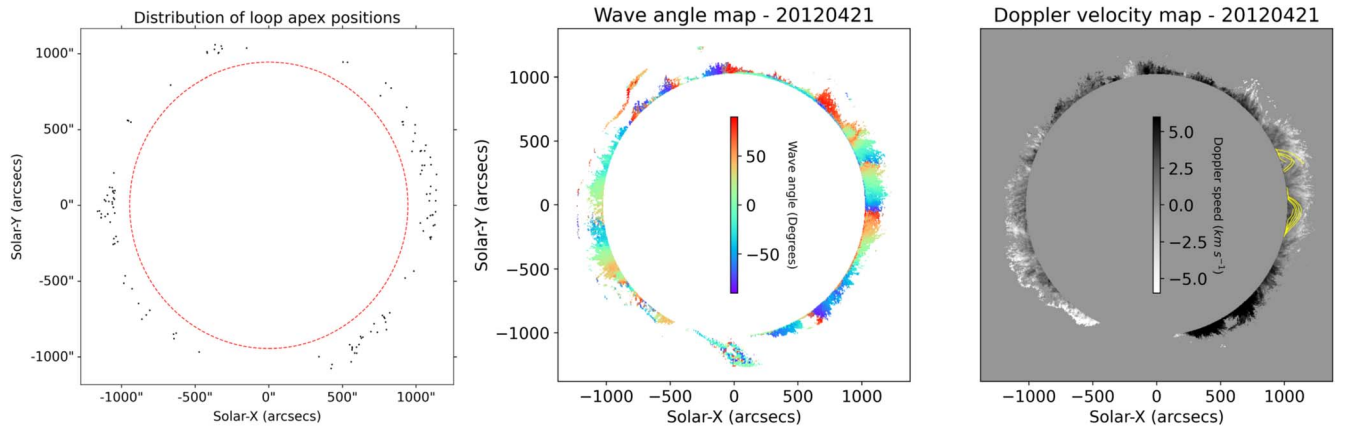


Figure 1. The left panel shows the position of all loops analyzed. The black dots correspond to the position of the loop apex. The red dashed lines represents the solar disk. A sample observation for the loops observed on 2012 April 21 are shown in the two right panels of the figure. The center panel shows the calculated wave angle at each pixel position, determined using a coherence-based method on each pixel of the Doppler velocity image. This wave angle serves as the guide for the tracks shown in yellow in the right panel.

The second criteria for loop selection require that the loops should be oriented such that the longitudinal direction of the magnetic field is close to being positioned in the plane of sky. The geometry and orientation of the loops are identified by performing magnetic field extrapolations using the potential field source surface (PFSS; Schrijver & DeRosa 2003) software. The PFSS extrapolations were performed using line-of-sight magnetogram data obtained from SDO’s Helioseismic and Magnetic Imager (Scherrer et al. 2012). The extrapolations provide us with a schematic geometry and orientation of the loops in the plane of sky. The extrapolated field lines visibly agree with the loop structures observed in the coronal EUV images obtained by SDO/AIA and with the intensity images obtained by CoMP. Furthermore, the loops are selected to avoid loops within the cores of active regions (i.e., rooted in or near sunspots). Some of the trans-equatorial loops identified were located in the extended plage region of active regions on the visible solar disk. The observed loops are assumed to be rooted in network regions and are not part of active region loop systems. The left panel of Figure 1 displays the location of the apex positions, with respect to the solar limb, of all the loops used within this study.

Due to the low spatial resolution of CoMP, the effect of line-of-sight integration, and projection effects, there is an issue of disambiguation of individual loops in CoMP observations. Hence, the focus is on the wave signals in the system of coronal loops, as opposed to an individual structure.

2.3. Wave Parameter Estimation

For each system of coronal loops, a number of wave paths are extracted. A *wave path* is defined as being a contiguous set of pixels through the loop system, starting and finishing at the occulting disk. A pixel is selected within the loop system, and the wave angle map is utilized to map out a path, selecting the subsequent pixel based on the angle of propagation. The path is followed until the occulting disk is reached. A square boxcar median filter of width two pixels was applied to the wave angle map to try and suppress some of the noise and led to the improved tracing of wave paths. The pixel locations for each wave path are then used to extract the relevant velocities from the Doppler velocity images for each frame in the image sequence. A cubic interpolation maps the velocities from the

selected wave paths onto (x, t) space. For each wave path, the neighboring five wave paths on either side of the original wave path are also extracted. The result of this is time–distance diagrams along the coronal loops systems. The longer loops lead to additional issues when tracing them because the wave angle suffers from more significant uncertainties closer to the apex of these loops. This arises because the wave angle is being poorly estimated near the upper boundaries of the wave angle map, primarily due to lower signal to noise in these regions arising from fainter coronal emission. In such cases, only the wave path for half a loop is obtained. The half-loop length is defined for each loop, obtained by finding the point of inflexion for the traced trajectory of the wave path (except for the longer loops where only a half loop is already traced).

The Doppler velocity time–distance diagram for each half loop is subject to a two-dimensional Fourier transform. The Fourier components are used to separate the inward and outward components of the wave propagation and provide velocity power spectra as a function of wavenumber–frequency $(k - \omega)$.

The propagation speed for the waves is calculated in a manner similar to Tomczyk & McIntosh (2009), Morton et al. (2015, 2019), and Tiwari et al. (2019). It is straightforward to filter either the inward or outward waves from the Fourier-transformed Doppler velocity time–distance diagrams by setting Fourier components equal to zero. The inverse Fourier transform of the filtered Fourier components then provides a Doppler velocity time–distance diagram containing only the inward or outward propagating waves. The cross correlation between the time series at the center of the wave path and the neighboring time series along the path is calculated from these filtered Doppler velocity time–distance diagrams. The location of the peak of the cross-correlation function gives the time lag between the signals and is determined by fitting a parabola to the peak. The observed lags as a function of the position along the wave path are fit with a linear function, and the gradient gives the propagation speed of the wave.

A feature of the propagating kink waves that is of particular interest is to estimate is the observed damping of these waves. The damping can be measured through analysis of the power ratio of the outward to inward propagating waves, $P(f)_{\text{ratio}}$. As mentioned, this has been performed previously by a number of authors for a single case study (Verth et al. 2010; Verwichte

et al. 2013b; Pascoe et al. 2015; Tiwari et al. 2019; Montes-Solís & Arregui 2020).

The velocity power as a function of frequency for the inward, $P_{\text{in}}(f)$, and outward $P_{\text{out}}(f)$, component of the waves are obtained by summing the velocity power spectra in the k direction. For each loop, the inward and outward power spectra are averaged over the neighboring wave paths to suppress the variability in the power spectra. From this one-dimensional averaged wave power, the ratio of the outward to inward power, $\langle P(f) \rangle_{\text{ratio}}$, is determined by taking the ratio of the power at corresponding positive and negative frequencies.

Following Verth et al. (2010), the function to model the ratio of the power spectra is defined as follows:

$$\langle P(f) \rangle_{\text{ratio}} = \frac{P_{\text{out}}}{P_{\text{in}}} \exp\left(\frac{2L}{v_{\text{ph}} \xi} f\right), \quad (1)$$

where L is the half-loop length, v_{ph} is the propagation speed and ξ is the equilibrium parameter (or quality factor) that provides a measure of the strength of the wave damping. The factor $P_{\text{out}}/P_{\text{in}}$ can be interpreted as the ratio of the power entering the corona through each of the loop footpoints. We note that Equation (1) is only valid when WKB conditions are satisfied, i.e., the wavelength is less than the length scale of inhomogeneity along the loop (see, e.g., Soler et al. 2011). For a plasma of $T_e \approx 1.3$ MK, the scale height is $H \approx 61$ Mm. For the kink waves we report here, the wavelength is $\lambda \approx 140$ Mm for a wave with frequency $f = 3.3$ mHz. However, given these are initial measurements of the propagating kink waves, we will use Equation (1). The equilibrium parameter that will be estimated can be thought of as an average value along the loop.

Estimates for ξ are obtained by fitting the model power ratio given by Equation (1) to the data, using a maximum likelihood approach. The associated confidence intervals on the model parameters were estimated by utilizing the *Fisher information*. For a detailed discussion on the statistics of the power ratio and the maximum likelihood approach, see Tiwari et al. (2019, their Section 3.4).

3. Results and Discussion

In total propagating kink waves in 120 individual quiescent loops observed with CoMP are analyzed. For each loop, estimates for the loop length, the propagation speed, the power ratio at the loop footpoint ($P_{\text{out}}/P_{\text{in}}$), and the equilibrium parameter (ξ) are obtained. The various parameters that were obtained are listed in Table 2. In the following subsections, a summary of the main properties of the propagating kink waves is provided.

3.1. Loop Lengths

First, a summary of the typical wave-path lengths is provided, which is used as a proxy for the loop length. In the left panel of Figure 2, the distribution of the half-loop lengths is shown. The half-loop lengths for the traced coronal loops are in the range of 50–600 Mm. The distribution peaks at around 150–200 Mm, and most of the loops observed are between 50 and 250 Mm. The number of longer loops is low, as it becomes increasingly difficult to trace the longer loops due to the limited FOV of the CoMP instrument. As well as the mentioned issue with visibility of the lower portions of the loops, the observed loop lengths suffer from projection effects, although it is hoped

that the selection criteria for the loops minimize this (see Section 2.2). Due to the reasons mentioned above, in the case of propagating waves, a loop length always means half the loop length.

3.2. Propagation Speeds

The distribution of propagation speeds is shown in the right panel of Figure 2, with the measured speeds distributed between 200 and 800 km s^{−1} and peaking around 400–600 km s^{−1}. This is consistent with the various propagation speeds reported in the literature (Tomczyk et al. 2007; Tomczyk & McIntosh 2009; Liu et al. 2014; Morton et al. 2015; Tiwari et al. 2019; Yang et al. 2020a, 2020b). The propagation speed values obtained are averaged over the outward and inward wave propagation speeds. There is some evidence that the outward and inward velocities are different, which can be explained by the presence of flows along the coronal loops. However, the methodology for the measurement of the wave propagation speed is currently not sensitive enough to quantify this, apart from in extreme cases (e.g., in coronal holes, see, Morton et al. 2015). The presence of flows leads to modification of the resonant damping of the kink waves, as described by Soler et al. (2011); consequently, this would require a change in the model for the power ratio that has been used. However, the influence of flows is neglected until they can be inferred more readily.

3.3. Power Ratio

The power ratio factor, $P_{\text{out}}/P_{\text{in}}$, defined in Equation (1) is essentially a measure of the power of the waves entering the corona at each footpoint of the loops. The distribution of the estimated values of power ratio is shown in the left panel of Figure 3, and has a mean value of 1.29 ± 0.04 . While the footpoint power ratio does not provide any information about the driving mechanism, it can be used as a proxy for measuring the energy input at each footpoint of the loop. The driving mechanism of propagating kink waves are thought to be one that acts globally due to the ubiquitous nature of these waves (Morton et al. 2019). Hence, one would expect that the energy entering the corona through each footpoint will be approximately equal, unless each set of footpoints is located in regions with dissimilar magnetic field strengths. The mean value of the footpoint power ratio supports this hypothesis and is in agreement with the results from previous studies (Verth et al. 2010; Tiwari et al. 2019). The scatter around the value of 1 could indicate that in some regions of the atmosphere, the driver is weaker/stronger than in others.

However, examination of the behavior of the power ratio as a function of the length of the coronal loop reveals the footpoint power ratio exhibits a decreasing trend with loop length (right panel of Figure 3). The power ratio starts at values close to 1.5 for the shorter loops and tends toward one as the loop length increases. A potential explanation for this trend could be that, for shorter loops, the wave power injected at each footpoint is different, possibly due to different excitation mechanism or due to differences in the frequency/strength of the driver. Why this should be the case for shorter loops only is not evident.

Instead, it is suggested that the enhanced power ratio for shorter loops is an artifact of the analysis method. If the spatial wavelength of the oscillation is on the order of, or greater than, the length of the wave path used in the analysis, then there can

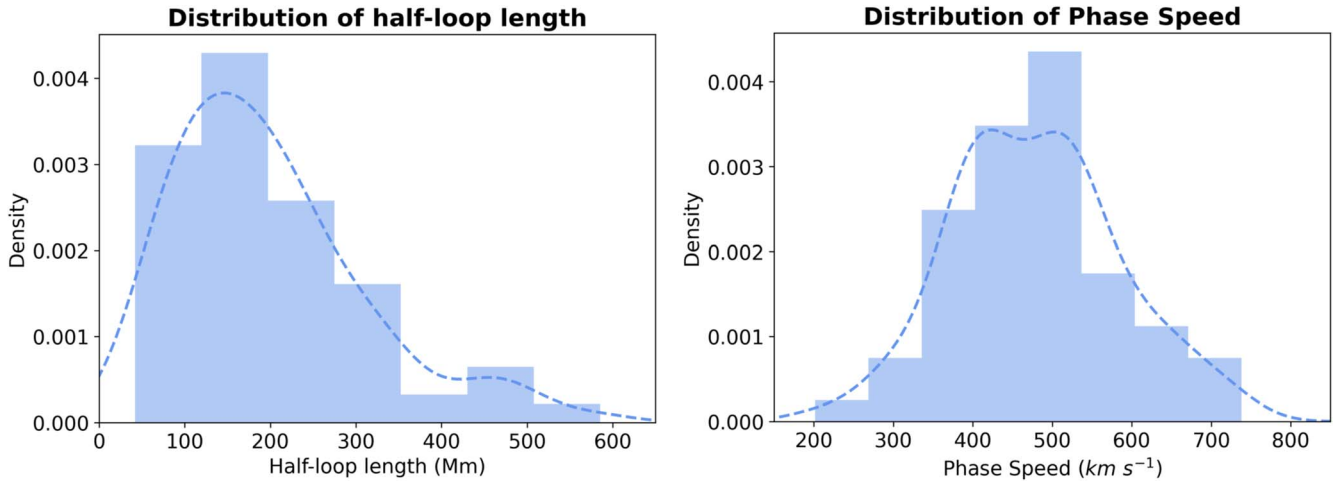


Figure 2. The left panel shows the distribution of measured half-loop lengths. The right panel corresponds to the measured phase speeds for the observed propagating waves. The blue bars and line represent the histogram and kernel density estimate (KDE) estimates for the distributions, respectively.

be a leakage of power into negative/positive values of k . As an example, the wavelength of the kink modes is $v_{ph} P$, where v_{ph} is the phase speed, and P is the period. Using the values associated with the observed waves, a period of 300 s and phase speed in the range of 200–600 km s^{-1} then gives wavelengths in the range of 60–180 Mm. Hence, the wavelengths are comparable to the lengths of the shorter loops selected here. The leakage of power from one quadrant of the power spectrum to another might be able to explain the observed deviation from 1. In future work, analysis can be modified to negate the impact of this power leakage, which can be avoided by fitting the power spectrum in ω – k space instead of just frequency.

3.4. Equilibrium Parameter

Perhaps the most interesting parameter estimated here is the equilibrium parameter or quality factor (ξ), which quantifies the damping rate of the waves. The distribution of ξ presented in the left panel of Figure 4 for the positive values. The values of ξ are between 0.89 and ~ 298 ; hence, they occupy a wide range of values (relative to the standing modes, see Morton et al. 2021). The distribution illustrates that $\sim 80\%$ of the positive ξ observations fall in the range of (0.89, 30). Hence, the propagating kink waves can be strongly damped or very weakly damped. The median value is ~ 11 , and a mean value of ~ 18 , which is greater than that found for the standing kink modes (see, Morton et al. 2021, for a full discussion of the importance of the observed values of the equilibrium parameter).

It should also be noted that of the 108 loops identified and studied, 31 of them show signs of power amplification, with a negative value of ξ . These are observed only for short loops (less than the half-loop length of 350 Mm). At present, it is unclear whether these results are physical. As already mentioned, short loops typically contain lower signal-to-noise velocity time series due to their proximity to the occulting disk. However, it has been shown by Soler et al. (2011) that flows can play an important role and can lead to amplification of waves. The amplification of waves is always in competition with wave damping mechanisms. However, as discussed, the values of ξ are typically large, which implies a weak damping. Hence, in loops with weak damping, there is an improved

chance to observe any amplification that may arise from flows or other mechanisms. These shorter loops with negative ξ need further investigation.

3.5. Equilibrium Parameters Relationship with Half-loop Length

Tiwari et al. (2019) gave evidence in favor of dependence between the equilibrium parameter (ξ) and the loop length, although there were only seven loops analyzed in that study. The additional measurements made here enables us to examine this dependence further. As mentioned, the loops selected for this study correspond to loops being oriented such that the longitudinal axes are predominantly in the plane of sky. It implies that the longer loops reach higher altitudes in the corona. The right panel of Figure 4 displays a scatter plot, revealing a range of equilibrium parameters are possible for all loop lengths. The equilibrium parameter also shows a distinct behavior with increasing loop length. As indicated by the results in Tiwari et al. (2019), as loop length increases, there is an increase in the value of the damping equilibrium parameter.

In order to show this relationship, whether several simple models of the form $\hat{\xi} = f(L)$ could describe the data is examined. The models examined were constant, linear, quadratic, square root, and log. Each model also contained a constant term. The models were fit to the data assuming that a normal distribution describes the likelihood of the data; hence, the negative log-likelihood of the form is minimized:

$$-2 \ln \mathcal{L} = \sum_{i=1}^N \frac{(\xi_i - \hat{\xi}(L))^2}{\sigma_i^2},$$

where ξ_i is the observed value, $\hat{\xi}(L)$ is the model prediction, and σ_i is the uncertainty on ξ_i . The out-of-sample prediction error is estimated to test the ability of each model to describe the data. First, leave-one-out cross validation is utilized, using the mean value of the negative log-likelihood as a measure of the test error. It turns out all models (except the constant) show a similar ability to describe the data, with the quadratic and linear models performing the best, although the difference between the nonconstant models is small. Moreover, the Akaike information criteria calculation supports the results

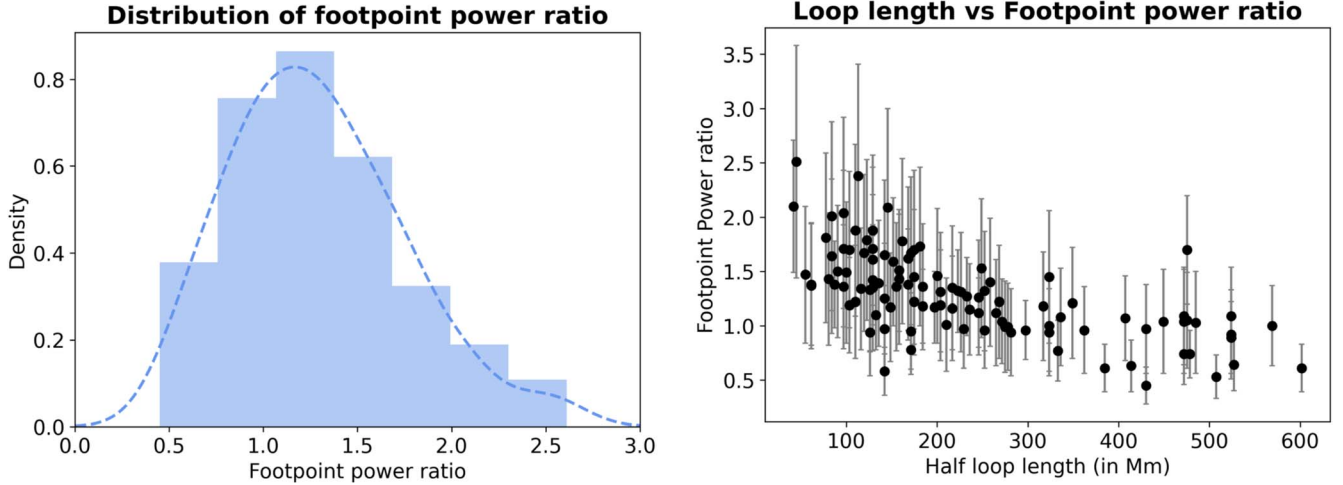


Figure 3. The left panel shows the distribution of measured footpoint power ratios after performing fitting for the observed waves. The blue bars and line represent the distribution and KDE for the footpoint power ratio for propagating kink waves. The right panel highlights the variation of footpoint power ratio with respect to the half-loop length. The black circles represent the footpoint power ratio, and the corresponding error bars are shown in gray.

from cross validation and confirms that the constant model performs the worst.

In the right panel of Figure 4, the results from the quadratic model is displayed. The uncertainty on the model curve is calculated by performing 10,000 bootstrap simulations of the fitting procedure, then using the percentile method to estimate the point-wise confidence intervals. The increase in ξ with loop length is evident. It is noted that the data also appear to show there is a lower bound to the possible values of ξ for the loops that increases with loop length.

The implication of the increase in ξ with loop length is that the propagating kink waves are subject to a reduced rate of damping for longer loops. As discussed in Tiwari et al. (2019), a physical explanation for the apparent decrease in damping rates can be made. Assuming that resonant absorption is the mechanism acting to provide the observed frequency-dependent damping, the quality factor for kink modes is given by

$$\xi = \alpha \frac{R \zeta + 1}{l \zeta - 1}, \quad (2)$$

where R is loop radius, l is the thickness of the density inhomogeneity layer, $\zeta = \rho_i/\rho_e$ is the ratio of the internal and external densities of the magnetic flux tube, respectively, and α is a constant whose value describes the gradient in density across the resonant layer. It is suggested that the key factor in understanding the observed behavior would be the density ratio between the internal and external plasma. Quiescent coronal loops should be subject to similar heating rates; hence, the rate of associated chromospheric evaporation is similar. If this is true, then the average density of the longer loops is likely to be less than those of shorter loops. This will lead to the density ratio (ρ_i/ρ_e) for longer loops being, on average, smaller than for the shorter loops compared to the ambient plasma.

As a basic examination of this premise, the scaling laws for dynamic loops derived in Bradshaw & Emslie (2020) are utilized. The scaling laws are derived under the assumption that a dynamic loop (i.e., one subject to heating) has reached a steady state, with the sum of the static pressure and dynamic pressure (arising from flows) being constant along the loop. The static pressure, temperature, and density vary along the

loop, but gravity is neglected. Moreover, it is assumed that the loops have a constant cross section along their length. The scaling laws are likely more applicable to short loops, where the hydrostatic scale height is on the order of the loop height. As mentioned earlier, for a plasma of $T_e \approx 1.3$ MK, the scale height is $H \approx 61$ Mm. The CoMP loops typically reach a higher altitude than this (see Figure 2 and Table 1); hence, the dynamic scaling laws are likely insufficient to describe the plasma conditions in the observed loops. Nevertheless, as there is no alternative, we use the scaling laws from Bradshaw & Emslie (2020), but do not place too much significance on the results.

From Equation (45) in Bradshaw & Emslie (2020), the loop apex density, n_m , is related to the heating rate, E_H , by

$$n_m = [c(M)E_H L^{1/4}]^{4/7},$$

where L is the half-loop length, and $c(M)$ is a function of the Mach number. The heating rate is assumed constant along the loop. We rewrite this expression in terms of the energy flux, $F_H = E_H L$, giving,

$$n_m = [c(M)F_H L^{-3/4}]^{4/7}. \quad (3)$$

The loop number density can be thought of as a combination of an initial number density (n_0) (due to some basal heating, E_{H_0}), which is assumed to be equal to ambient plasma (n_e), plus an additional density, n_1 , from the evaporation of the chromospheric/transition region due to some heating event (E_{H_1}) associated with the loop, i.e.,

$$n_m = n_0(E_{H_0}) + n_1(E_{H_1}).$$

The density ratio ζ can be defined as

$$\zeta = \frac{n_m}{n_e} \quad (4)$$

$$= 1 + \frac{F_{H_1}^{4/7}}{(2.4 \times 10^{-15})^{4/7} M n_e} L^{-3/7}. \quad (5)$$

This expression suggests that the density ratio may depend upon the length of the coronal loop, with the over-density of the loop decreasing as the loop length increases.

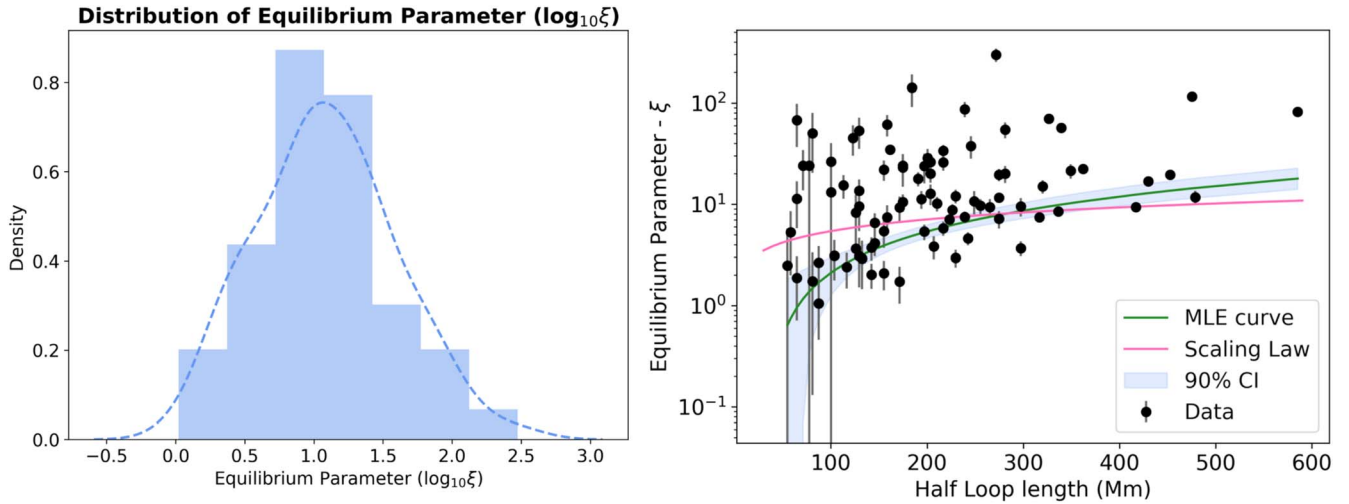


Figure 4. The left panel shows the distribution of estimated equilibrium parameter ξ . The blue bars and line represent the estimates for the distribution from the histogram and KDE methods, respectively. The right panel shows the dependence of the equilibrium parameter ξ on the half-loop length. The green curve shows the maximum likelihood estimate for a quadratic function of L , with the associated confidence intervals. The pink line is the potential variation in ξ from coronal loop scaling laws.

Table 1

Median Values of Various Characteristics of the Different Observed Kink Modes in the Solar Corona

Properties	Damped Standing	Damped Propagating	Decay-less Standing
Loop length (Mm)	324	349	190
Period (s)	7.3	...	4.2
Amplitude (Mm)	5	...	0.14
Equilibrium Parameter	1.8	11.4	...
Kink Speed (km s ⁻¹)	1336	483	1645

Note. In case of the propagating kink waves the loop length is calculated by multiplying the half-loop length by a factor of 2.

We then substitute the expression for ζ into Equation (2) to estimate the quality factor as a function of loop length. To obtain values of ξ , we require some reasonable estimates for quiet Sun parameters. Hence, we assume that: the energy flux is $F_H \approx 200 \text{ W m}^{-2} = 2 \times 10^5 \text{ erg s}^{-1} \text{ cm}^{-2}$; the electron density is $n_e = 10^{8.5} \text{ cm}^{-3}$; the Mach number is 0.1 (corresponding to flows of $\sim 10 \text{ km s}^{-1}$); $\alpha = 2/\pi$; and $l/R = 1$. The dependence of the quality factor on loop length from the scaling law theory is shown in Figure 4. While it does not match the curve from the model fitting, the results support our physical explanation for an increase in the equilibrium parameter as a function of loop length.

It is always worthwhile drawing comparisons between related results. To our knowledge, there is only one previous estimate for the damping rate of Alfvénic modes in the quiescent corona (excluding Verth et al. 2010; Tiwari et al. 2019), which was estimated in Hahn & Savin (2014).⁵ They provide estimates for the damping lengths of the waves, finding a broad distribution (up to 500 Mm) with a median value between 100 and 200 Mm. In order to provide a comparison to

their results, the estimated quality factors should be converted to damping lengths. The damping length (L_d) can be calculated using

$$L_d = \xi \lambda_{\text{prop}},$$

where $\lambda_{\text{prop}} = v_{\text{ph}} P$. Substituting typical values of the period (P) of the waves observed by CoMP (100–1000 s) and the measured phase speeds (see Table 2) in this expression given the damping lengths. Figure 5 shows the estimated damping lengths as a function of the period for three different values of v_{ph} , using the median value of ξ from measurements in this study. The damping lengths reported in Hahn & Savin (2014) are comparable to the estimated damping lengths for the shorter period waves from the CoMP observations (Figure 5). The damping lengths given by Hahn & Savin (2014) will themselves, of course, be related to waves with a particular range of periods. However, it is not straightforward to ascertain the periods of the waves encapsulated in the nonthermal line widths.

A value of ξ from the information in Hahn & Savin (2014) can also be estimated. Although the assumed values of propagation speed, v_{ph} , are not given in Hahn & Savin (2014), by inverting the given equation for the energy flux, F , namely,

$$F = \rho \langle \delta v^2 \rangle v_{\text{ph}},$$

where $\langle \delta v \rangle$ is the velocity amplitude from the nonthermal widths, gives the propagation speed. The given values of energy flux ($5.5 \times 10^5 \text{ erg s}^{-1} \text{ cm}^{-2}$), nonthermal widths (30 km s^{-1}), and electron density ($5 \times 10^8 \text{ cm}^{-3}$) are also utilized to find $v_{\text{ph}} = 550 \text{ km s}^{-1}$. Hence, using the damping lengths of 100–200 Mm, the quantity $\xi P = 180\text{--}360 \text{ s}$. The Hinode/EIS data used in their study is integrated over 60 s. Assuming that only waves with periods less than 60 s contribute to the line broadening (which is a very conservative assumption), then $\xi = 3\text{--}6$. These values are likely overestimates for their study (i.e., Hahn & Savin 2014) but are

⁵ In Hahn & Savin (2014), measurements of nonthermal line widths from Hinode/EIS data are assumed to represent Alfvénic waves. It is likely that the nonthermal broadening is due to the under-resolved kink waves, e.g., McIntosh & De Pontieu (2012), Pant et al. (2019)

Table 2
Measured Loop Parameters and Wave Parameters Obtained from Observations

Loop No.	Solar-X (arcsec)	Solar-Y (arcsec)	Date (YYYYMMDD)	Half-loop Length (in Mm)	ξ	Power Ratio	Phase Speed (km s ⁻¹)
1	798.50	-819.50	2012 Apr 23	42.0 ± 3.23	-1.53 ± 1.27	2.1 ± 0.61	291 ± 2
2	-1026.30	-238.20	2012 May 14	42.0 ± 3.23	-8.04 ± 5.78	2.17 ± 0.72	415 ± 15
3	980.56	422.56	2012 Jun 26	45.0 ± 3.23	-0.95 ± 2.07	2.51 ± 1.07	561 ± 11
4	-928.26	-549.67	2012 Jun 26	45.0 ± 3.23	-1.89 ± 2.0	2.51 ± 1.07	561 ± 11
5	-1136.86	-57.01	2012 Apr 10	55.0 ± 3.23	2.49 ± 3.23	1.47 ± 0.63	373 ± 4

(This table is available in its entirety in machine-readable form.)

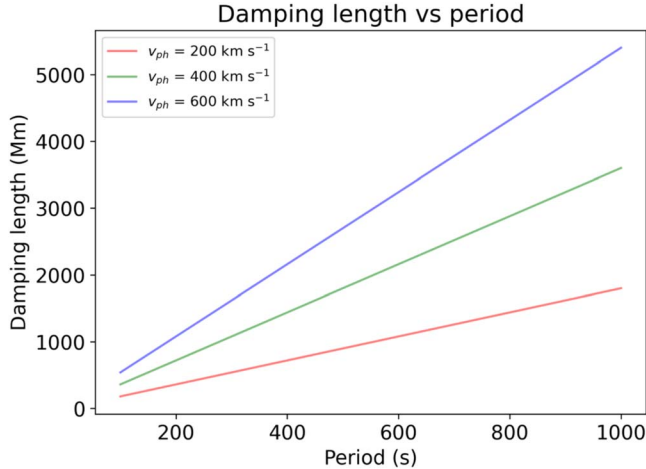


Figure 5. Estimated variation of damping length with phase speed, calculated using typical values for the period, and the median value of the equilibrium parameter.

broadly in agreement with the range of values found in this study (e.g., Figure 4).

3.6. Comparison with Observations of Different Modes of Kink Waves

Before concluding, we provide a light-touch comparison between the properties of the propagating kink waves observed here and the previous studies of the two standing kink modes, i.e., damped and decay-less. The comparison is worthwhile to highlight that the standing and propagating modes are found in coronal loops with significantly different plasma conditions.

For the damped standing kink waves, the catalog of events compiled by Goddard et al. (2016) and Nechaeva et al. (2019), using data from SDO/AIA is used. All the observations from these data sets, which did not have any associated period or damping time information, are removed. The total number of cases after this selection is 103 events over the course of solar cycle 23.

In the catalog of standing kink waves, the loop length is estimated under the assumption that the loops are close to the semicircular shape by either measuring the projected distance between the footpoints or by the apparent height. For each oscillation, the amplitude of the initial displacement and initial oscillation amplitude was given, along with the period. The mode of the standing kink waves here is assumed to be the fundamental.

The kink speed, which is not provided in the catalog of Nechaeva et al. (2019), is calculated as follows:

$$c_{\text{kink}} = \frac{\omega}{k} = \frac{4L}{P}, \quad (6)$$

where c_{kink} is the kink speed, L is the half-loop length, and P is the period of the waves observed. Furthermore, the equilibrium parameter is also calculated by using the measured damping time of the oscillations and the periods, i.e., $\xi = \tau/P$.

For the decay-less kink waves, the catalog put together by Anfinogentov et al. (2015, see their table A.1)⁶ is used. The catalog provides a study of 71 observations of decay-less kink waves in 21 active regions (NOAA 11637–11657) between 2012 December and 2013 January.

From both catalogs, the median values for the loop length, period, amplitude, and kink speed (see Table 1) are shown.⁷ For the damped waves, the median value of the equilibrium parameter is also presented.

In terms of the length of coronal loops that support the oscillations, the loops studied in this paper here have a similar distribution to those from the damped and decay-less standing wave studies. The propagating kink wave catalog also contains several longer loops. The reader is reminded that the loop lengths measured by CoMP and SDO/AIA are not directly comparable. The CoMP instrument has an occulting disk that obscures the corona below 1.05 R_{Sun} . Hence, the measurements for the coronal loops' length do not begin near the footpoints, and it is likely an underestimation of the length of the CoMP loops (a rough correction being the addition of 70 Mm to the given values). On the other hand, SDO/AIA images show the solar disk, often making the coronal footpoints of the loop visible in the images.

One of the main difference between the two loop populations is the measured kink speed. In the case of standing waves, the estimated kink speeds have medians of ~ 1300 and ~ 1700 km s⁻¹ for damped and decay-less, respectively. While for the propagating waves, the median value of the propagation speed is substantially smaller at ~ 480 km s⁻¹. The contrast of these values reflects the sizeable differences in the magnetic field strengths between the regions where these waves are observed (and also somewhat the different densities). The electron density in the quiet Sun (10^{8-9} cm⁻³) is less than that of active regions (10^{9-10} cm⁻³), which indicates the magnetic

⁶ The table was scraped using the BeautifulSoup module (Richardson 2007).

⁷ The loop length in case of the standing and the decay-less kink waves are the full semicircular loop lengths as seen in AIA/SDO, while in the case of the propagating kink waves the loop lengths refer to the half-loop length as seen in the CoMP FOV.

field strength must be substantially weaker in the quiescent Sun. This is borne out by estimates of the magnetic field strength, which in the active region coronal loops lies in the range of 4–30 G (e.g., Nakariakov & Ofman 2001; White & Verwichte 2012),⁸ while the magnetic field of the quiet Sun loops are estimated to be between 1 and 9 G (Morton et al. 2015; Long et al. 2017; Yang et al. 2020a, 2020b).

The difference in plasma parameters will ultimately bring about differences in how the waves/oscillations evolve as a function of time and/or distance. In fact, in the companion paper, Morton et al. (2021), a comprehensive discussion on the implications of differences in the equilibrium parameter found for the standing waves ($\xi_{\text{median}} = 1.8$) and the propagating waves ($\xi_{\text{median}} = 11.4$) is provided.

4. Summary and Conclusion

The details of a catalog of quiescent coronal loops observed with the CoMP instrument are provided, all of which show evidence for the presence of propagating kink waves. The catalog is used to undertake a statistical study of the propagating kink waves providing estimates for the damping rate and propagation speeds of the waves, presenting some details of how the propagating kink waves evolve. It is found that the equilibrium parameter, which quantifies the degree of wave damping, has a broad range of values, which indicates that in some of the coronal loops, the propagating kink waves are only weakly damped (this is aspect is discussed further in Morton et al. 2021). The damping length of the propagating kink waves is also estimated, which is found to be broadly comparable to the previous estimates of Hahn & Savin (2014). Moreover, the study also finds that there is a relationship between the degree of damping and loop length, with waves propagating along longer loops typically experiencing reduced damping, verifying claims of Tiwari et al. (2019). The suggested reason for this behavior is related to longer loops having a lower average density contrast, potentially due to limits on the amount of mass that can be evaporated during heating events associated with a given heating rate. Our analysis also finds signatures of the amplification of waves, the nature of which is unclear at this time.

A brief comparison of the observed properties of the propagating waves to the standing modes is also presented. Notable differences between propagation speed and damping rates are found, with the contrast being due to the dissimilar plasma and magnetic environments of the two populations of loops that support the waves. The standing kink waves have been reported predominantly in loops with at least one footpoint in an active region; however, the propagating kink waves have been reported to be ubiquitous in the solar corona.

It is envisaged that the catalog of propagating kink waves will provide the community with the foundation for further study of propagating kink waves in the quiet solar corona.⁹ Many potential studies can exploit the propagating kink waves to further probe the plasma conditions in the quiescent loops, with the potential to incorporate density measurements from the Fe XIII line pair that CoMP also observes and provide estimates of magnetic field and flows through magneto-seismology (Morton et al. 2015; Yang et al. 2020a). This will




ultimately enable us to develop a clear picture of how the propagating kink waves evolve in the quiescent corona and determine their role in plasma heating. Moreover, it is emphasized that there is a need for 3D MHD simulations of kink wave propagation in quiescent coronal loops to aid our understanding of the role of resonant absorption in the damping of propagating kink waves.

We would like to acknowledge Tom Van Doorselaere, Norbert Magyar, Marcel Goossens, and Stephen Bradshaw for valuable discussions. A.K.T. is supported by the European Union’s Horizon 2020 research and innovation program under grant agreement No. 824064 (ESCAPE¹⁰). R.J.M. is supported by a UKRI Future Leader Fellowship (RiPSAW—MR/T019891/1). J.A.M. is supported by the Science and Technology Facilities Council (STFC) via grant No. ST/T000384/1. The authors acknowledge the work of the National Center for Atmospheric Research/High Altitude Observatory CoMP instrument team. The authors also acknowledge STFC via grant No. ST/L006243/1 and for IDL support.

Appendix

Compilation of the loop parameters for the study of damped propagating kink waves in the solar corona.

ORCID iDs

Ajay K. Tiwari  <https://orcid.org/0000-0001-6021-8712>
 Richard J. Morton  <https://orcid.org/0000-0001-5678-9002>
 James A. McLaughlin  <https://orcid.org/0000-0002-7863-624X>

References

- Anfinogentov, S., Nisticò, G., & Nakariakov, V. M. 2013, *A&A*, **560**, A107
 Anfinogentov, S. A., Nakariakov, V. M., & Nisticò, G. 2015, *A&A*, **583**, A136
 Aschwanden, M. J., Fletcher, L., Schrijver, C. J., & Alexander, D. 1999, *ApJ*, **520**, 880
 Aschwanden, M. J., Nightingale, R. W., Andries, J., Goossens, M., & Van Doorselaere, T. 2003, *ApJ*, **598**, 1375
 Bradshaw, S. J., & Emslie, A. G. 2020, *ApJ*, **904**, 141
 Cally, P. S. 2017, *MNRAS*, **466**, 413
 Cranmer, S. R. 2018, *ApJ*, **862**, 6
 Cranmer, S. R., & Van Ballegooijen, A. A. 2005, *ApJS*, **156**, 265
 DeForest, C. E., & Gurman, J. B. 1998, *ApJL*, **501**, L217
 De Moortel, I., Ireland, J., & Walsh, R. W. 2000, *A&A*, **355**, L23
 Erdélyi, R., Doyle, J. G., Perez, M. E., & Wilhelm, K. 1998, *A&A*, **337**, 287
 Goddard, C. R., Nisticò, G., Nakariakov, V. M., & Zimovets, I. V. 2016, *A&A*, **585**, A137
 Goossens, M., Andries, J., & Aschwanden, M. J. 2002, *A&A*, **394**, L39
 Hahn, M., & Savin, D. W. 2014, *ApJ*, **795**, 111
 Handy, B. N., Acton, L. W., Kankelborg, C. C., et al. 1999, *SoPh*, **187**, 229
 Hollweg, J. V. 1984, *ApJ*, **277**, 392
 Ionson, J. A. 1978, *ApJ*, **226**, 650
 Katsiannis, A. C., Williams, D. R., McAteer, R. T. J., et al. 2003, *A&A*, **406**, 709
 Kohutova, P., Verwichte, E., & Froment, C. 2020, *A&A*, **633**, L6
 Lemen, J. R., Title, A. M., Akin, D. J., et al. 2012, *SoPh*, **275**, 17
 Liu, J., McIntosh, S. W., Moortel, I. D., Threlfall, J., & Bethge, C. 2014, *ApJ*, **797**, 7
 Long, D. M., Valori, G., Pérez-Suárez, D., Morton, R. J., & Vázquez, A. M. 2017, *A&A*, **603**, A101
 Magyar, N., Doorselaere, T. V., & Goossens, M. 2019, *ApJ*, **882**, 50
 Marsh, M. S., Walsh, R. W., & Bromage, B. J. I. 2002, *A&A*, **393**, 649
 McIntosh, S. W., & De Pontieu, B. 2012, *ApJ*, **761**, 138
 McIntosh, S. W., de Pontieu, B., Carlsson, M., et al. 2011, *Natur*, **475**, 477
 McIntosh, S. W., de Pontieu, B., & Tomczyk, S. 2008, *SoPh*, **252**, 321

⁸ It should be noted that the magnetic field measurements obtained by coronal magneto-seismology provide an underestimate of the magnetic field values (Verwichte et al. 2013a).

⁹ The catalog in Table 1 is available as a csv file.

¹⁰ <https://projectescape.eu/>

- Montes-Solís, M., & Arregui, I. 2020, *A&A*, **640**, L17
- Morton, R., Tomczyk, S., & Pinto, R. 2016, *ApJ*, **828**, 89
- Morton, R. J., Tiwari, A. K., Van Doorselaere, T., & McLaughlin, J. A. 2021, arXiv:2105.11924
- Morton, R. J., Tomczyk, S., & Pinto, R. 2015, *NatCo*, **6**, 7813
- Morton, R. J., Verth, G., Jess, D. B., et al. 2012, *NatCo*, **3**, 1315
- Morton, R. J., Weberg, M. J., & McLaughlin, J. A. 2019, *NatAs*, **3**, 223
- Nakariakov, V. M., & Kolotkov, D. Y. 2020, *ARA&A*, **58**, 441
- Nakariakov, V. M., & Ofman, L. 2001, *A&A*, **372**, L53
- Nakariakov, V. M., Ofman, L., Deluca, E. E., Roberts, B., & Davila, J. M. 1999, *Sci*, **285**, 862
- Nechaeva, A., Zimovets, I. V., Nakariakov, V. M., & Goddard, C. R. 2019, *ApJS*, **241**, 31
- Nisticò, G., Nakariakov, V. M., & Verwichte, E. 2013, *A&A*, **552**, A57
- Ofman, L., & Aschwanden, M. J. 2002, *ApJL*, **576**, L153
- Ofman, L., Romoli, M., Poletto, G., Noci, G., & Kohl, J. L. 1997, *ApJL*, **491**, L111
- Pant, V., Magyar, N., Doorselaere, T. V., & Morton, R. J. 2019, *ApJ*, **881**, 95
- Pascoe, D. J., Wright, A. N., De Moortel, I., & Hood, A. W. 2015, *A&A*, **578**, A99
- Pesnell, W. D., Thompson, B. J., & Chamberlin, P. C. 2012, *SoPh*, **275**, 3
- Richardson, L. 2007, Beautiful soup documentation <https://beautiful-soup-4.readthedocs.io>
- Ruderman, M. S., & Roberts, B. 2002, *ApJ*, **577**, 475
- Scherrer, P. H., Schou, J., Bush, R. I., et al. 2012, *SoPh*, **275**, 207
- Schrijver, C. J., & DeRosa, M. L. 2003, *SoPh*, **212**, 165
- Schrijver, C. J., Title, A. M., Berger, T. E., et al. 1999, *SoPh*, **187**, 261
- Soler, R., Terradas, J., Verth, G., & Goossens, M. 2011, *ApJ*, **736**, 10
- Stepanov, A. V., Zaitsev, V. V., & Nakariakov, V. M. 2012, *PhyU*, **55**, A04
- Thurgood, J. O., Morton, R. J., & McLaughlin, J. A. 2014, *ApJL*, **790**, L2
- Tian, H., McIntosh, S. W., Wang, T., et al. 2012, *ApJ*, **759**, 144
- Tian, H., Tomczyk, S., McIntosh, S. W., et al. 2013, *SoPh*, **288**, 637
- Tiwari, A. K., Morton, R. J., Régnier, S., & McLaughlin, J. A. 2019, *ApJ*, **876**, 106
- Tomczyk, S., Card, G. L., Darnell, T., et al. 2008, *SoPh*, **247**, 411
- Tomczyk, S., & McIntosh, S. W. 2009, *ApJ*, **697**, 1384
- Tomczyk, S., McIntosh, S. W., Keil, S. L., et al. 2007, *Sci*, **317**, 1192
- Van Doorselaere, T., Goossens, M., Magyar, N., Ruderman, M. S., & Ismayilli, R. 2021, *ApJ*, **910**, 58
- Van Doorselaere, T., Li, B., Goossens, M., Hnat, B., & Magyar, N. 2020, *ApJ*, **899**, 100
- Verth, G., Terradas, J., & Goossens, M. 2010, *ApJL*, **718**, L102
- Verwichte, E., Nakariakov, V. M., & Cooper, F. C. 2005, *A&A*, **430**, L65
- Verwichte, E., Van Doorselaere, T., Foullon, C., & White, R. S. 2013a, *ApJ*, **767**, 16
- Verwichte, E., Van Doorselaere, T., White, R. S., & Antolin, P. 2013b, *A&A*, **552**, A138
- Wang, T., Ofman, L., Davila, J. M., & Su, Y. 2012, *ApJL*, **751**, L27
- Wang, T. J., Solanki, S. K., Curdt, W., et al. 2003, *A&A*, **406**, 1105
- Weberg, M. J., Morton, R. J., & McLaughlin, J. A. 2018, *ApJ*, **852**, 57
- Weberg, M. J., Morton, R. J., & McLaughlin, J. A. 2020, *ApJ*, **894**, 79
- White, R. S., & Verwichte, E. 2012, *A&A*, **537**, A49
- Williams, D. R., Mathioudakis, M., Gallagher, P. T., et al. 2002, *MNRAS*, **336**, 747
- Williams, D. R., Phillips, K. J. H., Rudawy, P., et al. 2001, *MNRAS*, **326**, 428
- Yang, Z., Bethge, C., Tian, H., et al. 2020a, *Sci*, **369**, 694
- Yang, Z., Tian, H., Tomczyk, S., et al. 2020b, *ScChE*, **63**, 2357
- Zimovets, I. V., & Nakariakov, V. M. 2015, *A&A*, **577**, A4